




Experimental and simulation study of the high-pressure behavior of squalane and poly- α -olefins

Cite as: J. Chem. Phys. **152**, 074504 (2020); <https://doi.org/10.1063/1.5139723>

Submitted: 22 November 2019 . Accepted: 30 January 2020 . Published Online: 18 February 2020

 Iain J. Prentice,  Xiaojiao Liu,  Oleg A. Nerushev, Sashi Balakrishnan,  Colin R. Pulham, and  Philip J. Camp



View Online



Export Citation



CrossMark

ARTICLES YOU MAY BE INTERESTED IN

[The dynamics of supercooled water can be predicted from room temperature simulations](#)

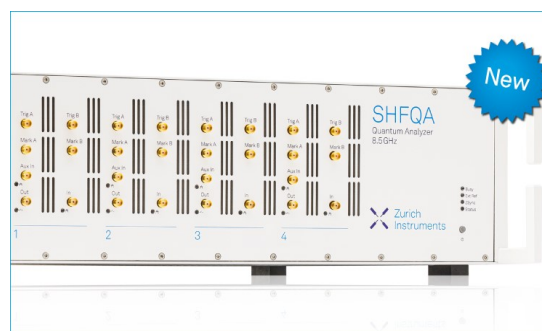
The Journal of Chemical Physics **152**, 074505 (2020); <https://doi.org/10.1063/1.5139435>

[Transport coefficients of model lubricants up to 400 MPa from molecular dynamics](#)

The Journal of Chemical Physics **152**, 191104 (2020); <https://doi.org/10.1063/5.0008907>

[Drying kinetics and nucleation in evaporating sodium nitrate aerosols](#)

The Journal of Chemical Physics **152**, 074503 (2020); <https://doi.org/10.1063/1.5139106>



Your Qubits. Measured.

Meet the next generation of quantum analyzers

- Readout for up to 64 qubits
- Operation at up to 8.5 GHz, mixer-calibration-free
- Signal optimization with minimal latency

Find out more



Experimental and simulation study of the high-pressure behavior of squalane and poly- α -olefins

Cite as: J. Chem. Phys. 152, 074504 (2020); doi: 10.1063/1.5139723

Submitted: 22 November 2019 • Accepted: 30 January 2020 •

Published Online: 18 February 2020



Iain J. Prentice,¹ Xiaojiao Liu,^{1,2} Oleg A. Nerushev,^{1,2} Sashi Balakrishnan,³ Colin R. Pulham,^{1,2} and Philip J. Camp^{1,a)}

AFFILIATIONS

¹School of Chemistry, University of Edinburgh, David Brewster Road, Edinburgh EH9 3FJ, Scotland

²Centre for Science at Extreme Conditions, University of Edinburgh, Peter Guthrie Tait Road, Edinburgh EH9 3FD, Scotland

³Global Lubricants Technology Research and Innovation, BP International Limited, Technology Centre, Whitchurch Hill, Pangbourne, Reading RG8 7QR, England

^{a)} Author to whom correspondence should be addressed: philip.camp@ed.ac.uk

ABSTRACT

The equation of state, dynamical properties, and molecular-scale structure of squalane and mixtures of poly- α -olefins at room temperature are studied with a combination of state-of-the-art, high-pressure experiments and molecular-dynamics simulations. Diamond-anvil cell experiments indicate that both materials are non-hydrostatic media at pressures above ~ 1 GPa. The equation of state does not exhibit any sign of a first-order phase transition. High-pressure x-ray diffraction experiments on squalane show that there are no Bragg peaks, and hence, the apparent solidification occurs without crystallization. These observations are complemented by a survey of the equation of state and dynamical properties using simulations. The results show that molecular diffusion is essentially arrested above about 1 GPa, which supports the hypothesis that the samples are kinetically trapped in metastable amorphous-solid states. The shear viscosity becomes extremely large at very high pressures, and the coefficient governing its increase from ambient pressure is in good agreement with the available literature data. Finally, simulated radial distribution functions are used to explore the evolution of the molecular-scale structure with increasing pressure. Subtle changes in the short-range real-space correlations are related to a collapse of the molecular conformations with increasing pressure, while the evolution of the static structure factor shows excellent correlation with the available x-ray diffraction data. These results are of indirect relevance to oil-based lubricants, as the pressures involved are comparable to those found in engines, and hence, the ability of lubricating thin films to act as load-bearing media can be linked to the solidification phenomena studied in this work.

Published under license by AIP Publishing. <https://doi.org/10.1063/1.5139723>

I. INTRODUCTION

In recent decades, the transportation industry has been dedicated to developing and implementing solutions for the reduction of CO₂ emissions, as well as for the improvement of the overall efficiency of fuel sources. This has involved increasing engine operating pressures in order to improve the engine efficiency, as well as developing new lubricants with different formulations of additives and base oils to reduce friction losses in the engines.^{1,2} There is a move toward lower-viscosity base oils

in order to reduce the inherent frictional losses in the lubricant and to decrease the thickness of the lubricant tribofilm at the interfaces between engine components.^{3–5} However, decreasing the thickness of the oil film significantly enhances engine wear, and this is made worse by the increasing engine operating pressures.^{4,6} In order to improve engine lubricant formulations—to meet strict international emission standards as well as to improve the wear protection—it is crucial to have a thorough understanding of the behavior of lubricants over the range of conditions typically found in engines.

This work focuses on studying the high-pressure properties of model lubricant base oils, using a combination of experimental techniques and molecular simulations. Estimates of the instantaneous pressures generated between metal surfaces within engines, gear boxes, and transmission systems are on the order of 0.2–5 GPa. From a thermodynamic perspective, the lowest free energy state of a normal pure substance at high pressure is a crystalline solid, while highly polydisperse mixtures may fractionate to form crystalline phases.⁷ Under confinement, simple liquids may crystallize,⁸ become disordered solids,⁹ or even remain viscous and liquid-like while retaining the ability to bear a load and sustain non-isotropic stresses.¹⁰ Here, the high-pressure behavior of some simple hydrocarbons is studied under bulk conditions. A particular focus is the crossover from a hydrostatic medium to a non-hydrostatic medium with increasing pressure. This phenomenon is well-known in the context of high-pressure experiments, where a hydrostatic liquid is required to ensure that the pressure exerted on a (solid) sample is isotropic. Various mixtures of simple organic and silicone oils are commonly used as pressure-transmitting media, but there will always be a pressure above which the liquid becomes a non-hydrostatic solid.^{11,12}

Base oils can come from a number of different base stocks and mainly consist of various mixtures of hydrocarbons with 18–40 carbon atoms, and either paraffinic or naphthenic molecular structures.¹³ As a starting point, it is helpful to focus on a single compound that is representative of the mixture. A major challenge associated with the molecular simulation of base oils is the complexity of the mixture, which would require a large total number of molecules in order to have each fraction represented adequately. Even from the experimental point of view, it is useful to focus on pure compounds so that the composition and properties are well-controlled and reproducible. Squalane (2,6,10,15,19,23-hexamethyltetracosane, $C_{30}H_{62}$)¹⁴ is widely used as a model compound to represent the fully saturated long-chain hydrocarbons in base oils. The molecular structure is shown in Fig. 1. Squalane is a valued cosmetic ingredient, as it is able to increase skin hydration due to the surface occlusions¹⁵ and it also naturally exists in small amounts in the lipid layers of skin.¹⁶ Furthermore, it exhibits certain bioactivity, which has applications in the nutraceutical and pharmaceutical industries.¹⁵ Therefore, understanding the properties of squalane not only is relevant to the lubricant industry but also benefits the cosmetic and pharmaceutical industries, particularly in the manufacturing process.

Data on the equilibrium phase behavior of squalane are sketchy. The freezing temperature of squalane at atmospheric pressure is

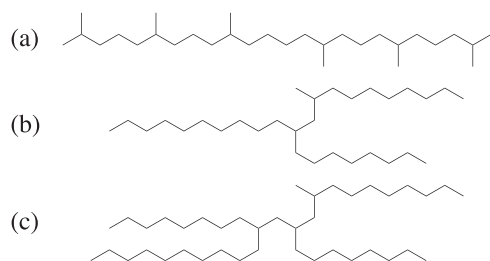


FIG. 1. Molecular structures of (a) squalane, (b) dec-1-ene trimer, and (c) dec-1-ene tetramer.

235 K.¹⁷ From molecular simulations by Porras-Vazquez *et al.*,¹⁸ the freezing pressure at 298.15 K is about 0.75 GPa. The equation of state and viscosity have been measured and fitted up to 0.2 GPa and over a range of temperatures.^{19,20} Bair and co-workers studied the viscosity of squalane at a range of temperatures and up to very high pressures ($P = 1.35$ GPa).^{21–23} The viscosity rises rapidly at high pressure, and based on extrapolations to a nominal threshold value (e.g., 10^{10} mPa s), it is possible to define a glass transition.²³ The glass transition is also signaled by features in the thermal conductivity and heat capacity as functions of temperature.²³ Hence, a glass-transition line can be superimposed on the equilibrium phase diagram. At ambient pressure, the glass-transition temperature is 174 K (from thermal conductivity/heat capacity) and 184 K (from viscosity).²³ An analysis of these data is presented in Sec. III A.

The experimental work herein employs state-of-the-art, high-pressure techniques to explore the properties of squalane at room temperature and pressures of up to several gigapascals. The primary goal is to explore the equation of state at the high pressures approached in engines. Some structural information is also obtained from *in situ* high-pressure x-ray diffraction (HPXRD). In the experiments, squalane is found to solidify without crystallization. Essentially, the material becomes a non-hydrostatic medium, but without long-range positional ordering of the constituent molecules.

Molecular-dynamics (MD) simulations are used to shed light on the “undercooled” regime, with this term referring to the fact that the temperature is lower than the equilibrium freezing temperature at high pressure. Using the fact that nucleation is a rare event and that complex molecules do not often crystallize spontaneously on simulation time scales, the MD calculations are used to explore the equation of state, and the structural and dynamical properties, of squalane in the high-pressure, undercooled regime. The simulation results are generally consistent with the experimental observations and provide molecular-scale insights into the solidification phenomenon.

There have been many simulation studies of the rheological properties of squalane, and these have mainly focused on the diffusion and (Newtonian) shear viscosity under ambient conditions,^{24,25} the non-Newtonian (shear-thinning) regime at high pressure,^{26–28} and the rheological and tribological properties of the confined fluid, either on its own,^{29–31} or with additives.^{32,33} In the MD work by Porras-Vazquez *et al.*,¹⁸ referred to above and discussed in Sec. III A, the liquid–solid phase boundary was sketched out over the temperature range 235–500 K and at pressures of up to about 5 GPa.

To demonstrate that other oil-like liquids may undergo a similar crossover to an amorphous solid at high pressure, some experimental and MD-simulation results are presented for a two-component mixture of trimers and tetramers of dec-1-ene or poly- α -olefins (PAOs), as shown in Fig. 1. A mixture with composition 80 wt. % $C_{30}H_{62}$ and 20 wt. % $C_{40}H_{82}$ is a reasonable model for group IV base oils. Existing experimental data are available for the pure dec-1-ene trimer,²¹ and these will be presented for comparison with the new results arising from the current work.

The rest of this article is organized as follows. The materials and methods are outlined in Sec. II, and this includes experimental work with diamond-anvil cells (DACs) (Sec. II B), high-pressure x-ray diffraction (Sec. II C), and simulation work using MD

(Sec. II D). A comprehensive set of results for squalane is presented in Sec. III, including experimental evidence for the solidification of squalane (Sec. III A), experimental and simulation measurements of the equation of state (Sec. III B), simulation measurements of the diffusion and shear viscosity (Sec. III C), and finishing with experimental and simulation results on the microscopic structure (Sec. III D). A short set of results for the PAO mixture is given in Sec. IV, and Sec. V concludes the article.

II. MATERIALS AND METHODS

A. Materials

Squalane was purchased from Sigma-Aldrich. The PAO mixture was provided by BP International Ltd. All experiments were conducted without further purification.

B. Diamond-anvil cell (DAC) experiments

A Merrill-Bassett diamond-anvil cell (DAC) with anvil culets of 600 μm diameter was used in all experiments. A stainless-steel gasket with an initial thickness of 250 μm was pre-indented to a thickness of 120 μm with a bore of 300 μm . The local pressure in different regions of the DAC was measured using the ruby fluorescence method^{34–36} in which the position of the R_1 line in the fluorescence emission spectrum depends on pressure in a known way. Ruby spheres were loaded into the DAC, and nine of them were randomly selected across the sample chamber (see Fig. 2). The ruby fluorescence was excited using an argon-ion laser (514.5 nm) and detected separately for each sphere with a CCD detector attached to a Jobin-Yvon Lab Raman 300 spectrometer. All experiments were carried out at room temperature ($T \approx 297$ K).

The position of the R_1 line was determined by a fit of the fluorescence spectrum using the Pearson VII distribution function.^{37,38} Pressures were then calculated using the standard ruby calibration method.³⁹ The standard deviation of the pressures was calculated from the local pressures P_i indicated by the $n = 9$ selected ruby spheres,

$$\sigma_P^2 = \frac{1}{n-1} \sum_{i=1}^n (P_i - \bar{P})^2, \quad (1)$$

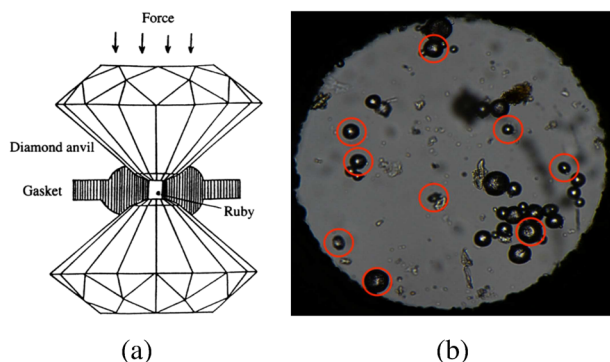


FIG. 2. (a) Schematic diagram of the DAC. The sample and ruby chips are confined by the gasket. (b) Photograph of the DAC sample volume loaded with squalane and ruby spheres. The nine rubies selected for fluorescence measurements are highlighted with red circles.

where $\bar{P} = \frac{1}{n} \sum_{i=1}^n P_i$ is the mean pressure.³⁶ In a hydrostatic medium, $\sigma_P \approx 0$ because liquids cannot support a non-isotropic stress. In a non-hydrostatic medium, such as in a solid, the local pressure can vary due to the lack of stress relaxation through the sample.

The equation of state was determined in separate experiments by determining the volume of the cavity, which is the product of the cavity area and height. The area was found from microscope images, while the height was found by measuring the distance between the external faces of the diamonds, and assuming that the compression of the diamonds is negligible. The measurement procedure will be described in detail elsewhere.⁴⁰ The loading of the material in the DAC was not known accurately, and so the density as a function of pressure was scaled so that it matches the experimental or simulated values under ambient conditions.

C. High-pressure x-ray diffraction (HPXRD)

High-pressure XRD (HPXRD) data were collected at synchrotron beamline I15, Diamond Light Source, UK, using a monochromatic x-ray beam with an incident wavelength of 0.424 600 Å. 2D diffraction images were collected at room temperature (~ 293 K) using a Perkin-Elmer 1621 detector. DAWN 2.11.0 software⁴¹ was used to integrate the 2D diffraction patterns as a function of d spacing to give one-dimensional diffraction profiles. Liquid squalane was loaded into a DAC with ruby spheres. The DAC was gently closed, with no pressure applied, and an HPXRD profile was measured. The pressure was then increased to 5.09 GPa, and another profile was measured.

D. Molecular-dynamics (MD) simulations

MD simulations were performed using Large-scale Atomic/Molecular Massively Parallel Simulator (LAMMPS).^{42,43} All of the simulations were carried out starting from a random configuration of 500 molecules; in the PAO mixture, this meant 429 trimers (79.9 wt. %) and 71 tetramers (20.1 wt. %). The initial random configurations were generated using Packmol.⁴⁴ The interactions of the molecules were given by the Optimized Potentials for Liquid Simulations (OPLS) force field,^{45–47} either the all-atom (AA) version or the united-atom (UA) version, in which CH, CH₂, and CH₃ groups are represented by united atoms. Both the AA and UA force fields were used for calculations of the equation of state, self-diffusion coefficient, and structural properties, while the viscosity was computed using the UA force field only due to computational constraints. All simulations were performed in a cubic cell with periodic boundary conditions. Lennard-Jones interactions were cut off at 10 Å, while the electrostatic interactions in the AA simulations were handled using the particle-particle particle-mesh Ewald method. The equations of motion were integrated with the velocity-Verlet algorithm.

The system was first equilibrated with a 0.2 ns simulation in the NVE ensemble using a time step of 0.1 fs. The energy was then minimized before moving on to a 10 ns run at $T = 298.15$ K and $P = 1$ atm using the Nosé-Hoover thermostat/barostat and a time step of 1 fs. Then, 30-ns NPT simulations at different pressures were carried out to determine properties such as the equation of state, radial distribution functions (RDFs), and self-diffusion coefficients.

The shear viscosity was calculated using non-equilibrium MD (NEMD) shearing simulations employing the SLLOD algorithm.^{48,49} A series of runs of 10–200 ns under constant-volume conditions were carried out over a range of (high) shear rates $\dot{\gamma}$, and the average shear stress in the shear (xy) plane was computed. The shear-rate dependent viscosity was then calculated using

$$\eta(\dot{\gamma}) = \frac{\langle P_{xy} \rangle}{\dot{\gamma}}. \quad (2)$$

Then, an Eyring equation was used to extrapolate the data to the limit $\dot{\gamma} \rightarrow 0$ to give an estimate of the Newtonian-regime viscosity $\eta = \eta(0)$,^{27,28,50}

$$\eta(\dot{\gamma}) = \eta(0) \left(\frac{2\dot{\gamma}_0}{\dot{\gamma}} \right) \ln \left[\left(\frac{\dot{\gamma}}{2\dot{\gamma}_0} \right) + \sqrt{1 + \left(\frac{\dot{\gamma}}{2\dot{\gamma}_0} \right)^2} \right]. \quad (3)$$

The UA force field was used for calculations of the shear viscosity, because of the simulation time required to obtain reasonable results. The simulations were carried out at $T = 298.15$ K and at the densities determined from the NPT simulations.

The Eyring equation is not the only choice for fitting the NEMD results, the Carreau equation being a viable alternative at lower pressures.^{27,28} Moreover, an “incremental” shear-rate dependent viscosity $\eta(\dot{\gamma}) = d\langle P_{xy} \rangle / d\dot{\gamma}$ may also be defined, which differs from the usual definition in the non-Newtonian regime, although Eq. (2) is used here. The reason for using NEMD simulations, as opposed to equilibrium MD simulations and the Green-Kubo or Einstein relations, is that at the very high pressures surveyed in this work, the relaxation times of equilibrium shear-stress fluctuations become extremely long, requiring very long simulations. Although the NEMD extrapolation procedure is not perfect, it does at least give reasonable results without immense computational cost.

III. RESULTS: SQUALANE

A. Hydrostatic limit from DAC experiments

There are several widely used ruby-fluorescence methods for detecting pressure-induced solidification, such as measuring the width of the R_1 line or the splitting of the R_1 and R_2 lines. Klotz *et al.* demonstrated that the most sensitive and reliable criterion is to measure the standard deviation of the pressures indicated by the R_1 lines of rubies distributed throughout the sample, as this directly quantifies the spatial variation of stress.³⁶ The results are shown in Fig. 3(a). Theoretically, for hydrostatic conditions, $\sigma_P = 0$ as all ruby spheres should be subjected to the same pressure. Small offsets are apparent at pressures up to about 1 GPa, which are caused by unavoidable instrumental and technique errors. Above 1 GPa, σ_P increases rapidly and roughly linearly with increasing pressure. The results were fitted using a simple piecewise analytic function, given by

$$f(P) = \begin{cases} f_0, & P < P^* - \Delta P \\ f_0 + \frac{f_1}{4\Delta P} [P - (P^* - \Delta P)]^2, & P^* - \Delta P \leq P < P^* + \Delta P \\ f_0 + f_1(P - P^*), & P \geq P^* + \Delta P. \end{cases} \quad (4)$$

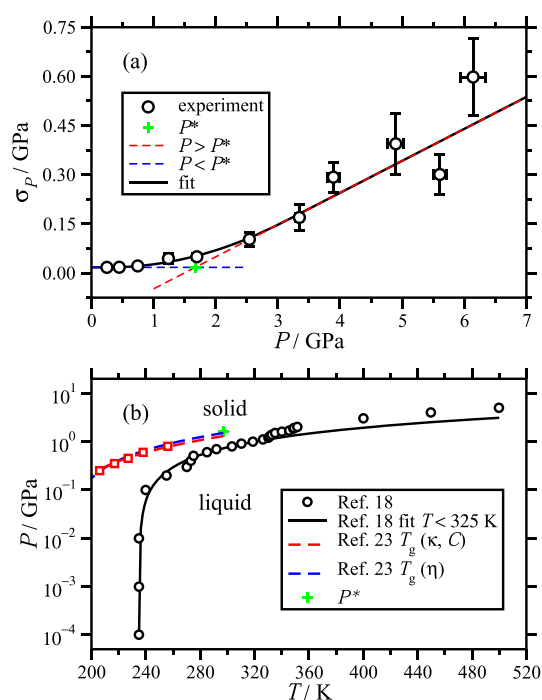


FIG. 3. (a) Pressure dependence of the standard deviation σ_P for squalane at $T \approx 297$ K. The black circles are from the experiment, and the solid black line is the fit from Eq. (4). The blue and red dashed lines show the limiting behavior at low pressure and high pressure, respectively, and the two intersect at $P^* \approx 1.7$ GPa, shown by a green cross. (b) Phase diagram of squalane. The black circles indicate the liquid–solid phase boundary from simulations presented in Ref. 18. The black solid line is a fit to the Clapeyron equation with a constant value of dP/dT over the temperature range $235 \text{ K} \leq T \leq 325 \text{ K}$. The red squares and red dashed line indicate the glass-transition line from thermal-conductivity and heat-capacity measurements presented in Ref. 23 and extrapolated to 297 K. The blue dashed line indicates the glass-transition line from viscosity measurements over the same temperature range.²³ The green cross (P^* at 297 K) indicates where the liquid begins to solidify in the current experiments.

This quadratic function interpolates between a constant value (for $P < P^* - \Delta P$) and a linear increasing function (for $P > P^* + \Delta P$) over the range $P^* \pm \Delta P$. Extrapolations of the two linear functions intercept at $P = P^*$. Fitting the experimental results gives $P^* = 1.67(48)$ GPa, $f_0 = 0.0175(25)$ GPa, $f_1 = 0.098(22)$, and $\Delta P = 1.40(65)$ GPa.

Figure 3(b) shows the liquid–solid phase boundary for squalane estimated from MD simulations by Porras-Vazquez *et al.*¹⁸ In those simulations, liquids were simulated at fixed pressure and a series of decreasing temperatures, and the liquid–solid phase transition was signaled by a change in the slope of the volume-temperature curve. If anything, these temperatures will be underestimates of the equilibrium liquid–solid phase boundary because solidification would be seen on the simulation time scale when the system is undercooled. Hence, the equilibrium boundary should be shifted slightly to the right of the line in Fig. 3(b), and at fixed temperature, the equilibrium freezing pressure should be lower than that indicated. Accurate phase boundaries can be determined by free-energy

calculations, but these would be computationally demanding for squalane. The solid line in Fig. 3(b) is a fit to the Clapeyron equation $dP/dT = \Delta S/\Delta V$, with the right-hand side being independent of temperature. There appears to be a kink in the data at around 325 K, and so the fit was restricted to $T \leq 325$ K, giving $\Delta S/\Delta V = 0.0117(3)$ GPa K⁻¹, and a freezing pressure of 0.74 GPa at 298.15 K. Including temperature corrections does not appreciably improve the fits and just leads to large uncertainties in the temperature-independent terms.

Figure 3(b) also shows the glass-transition lines presented by Bair *et al.*,²³ along with the pressure at which, in the current experiments, the liquid begins to solidify at 297 K. Extrapolations of the published glass-transition lines to 297 K give 1.30 GPa (from thermal conductivity/heat capacity) and 1.51 GPa (from viscosity). Notwithstanding the large error bar on P^* , and that it is unknown how σ_P should behave at the glass transition, there is good correspondence between current and published observations, indicating that the observed hydrostatic limit of squalane is associated with crossing the glass-transition line.

Before moving onto more detailed results, some simulation snapshots from NPT MD simulations are shown in Fig. 4. Images are shown for ambient conditions ($P = 10^{-4}$ GPa) and $P = 1$ GPa. In simulation movies, the dynamics are seen to be arrested above 1 GPa, and there is no sign of crystallization. These observations will be discussed in more detail in Secs. III C and III D.

B. Equation of state from DAC experiments and MD simulations

The experimental results in Sec. III A show that the pressure is not uniform throughout the compressed phase. Nonetheless, the equation of state can be explored by plotting the sample density against the average pressure. The results are shown in Fig. 5(a), scaled to give the known mass density of $\rho_0 = 805.4$ kg m⁻³ at standard pressure $P_0 = 1$ bar = 10^{-4} GPa and $T = 298.15$ K.²⁰

Mylona *et al.* used the Tait equation of state to fit experimental measurements at temperatures 273 K $\leq T \leq 473$ K and pressures up to 0.2 GPa,²⁰

$$\frac{\rho_0}{\rho} = 1 - A \log_{10} \left(\frac{B + P}{B + P_0} \right), \quad (5)$$

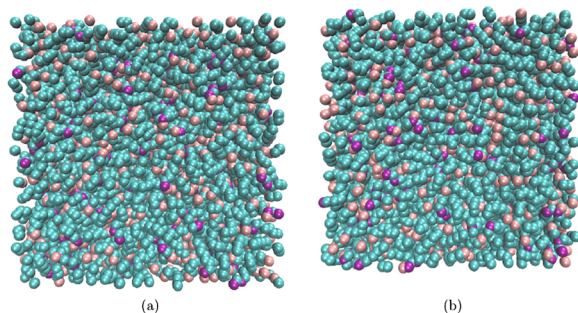


FIG. 4. Simulation snapshots of squalane at $T = 298.15$ K and (a) $P = 10^{-4}$ GPa and (b) $P = 1$ GPa using the UA force field. CH₃ united atoms are shown in gray, CH₂ united atoms are shown in blue, and CH united atoms are shown in purple.

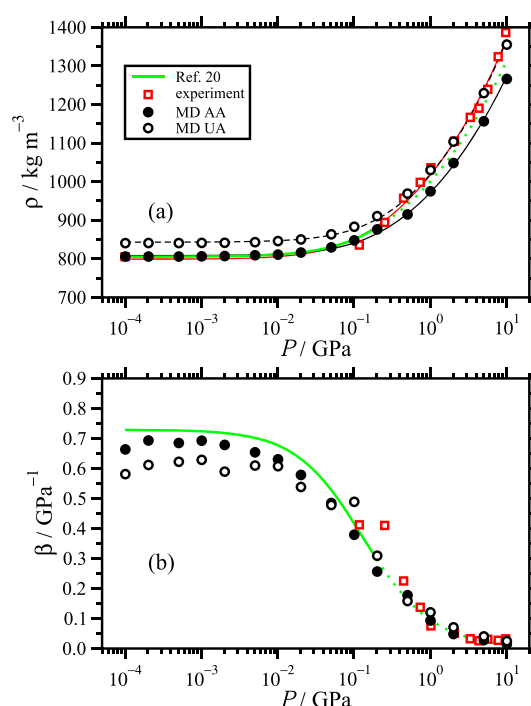


FIG. 5. The equation of state of squalane. (a) The mass density as a function of pressure. The green solid line is an experimental correlation up to 0.2 GPa,²⁰ and the green dotted line is an extrapolation to higher pressures. The other lines are fits using the Tait equation of state [Eq. (5)]. (b) The isothermal compressibility as a function of pressure. The green solid/dotted lines are from the literature correlation/extrapolation.²⁰ In both (a) and (b), the red squares are from the DAC experiments and the filled and unfilled black circles are from MD simulations with AA and UA force fields, respectively.

where $\rho_0/\text{kg m}^{-3} = 996.28 - 0.6402 T/\text{K}$ is the temperature-dependent mass density at the standard pressure of P_0 , and A and B are independent of pressure. The coefficients given by Mylona *et al.* are shown in Table I. The “correlation” refers to the fit up to 0.2 GPa, and the “extrapolation” refers to the continuation to higher pressures. Both are shown in Fig. 5(a).

TABLE I. Fit parameters to experimental and MD simulation results for squalane and PAOs at $T = 298.15$ K. ρ_0 , A , and B are the parameters in the Tait equation of state [Eq. (5)]. Where indicated, the figure in brackets is the estimated uncertainty in the final digits.

Material	Source	ρ_0 (kg m ⁻³)	A	B (GPa)
Squalane	Reference 20	805.4	0.20	0.119 110
Squalane	Experiment	799(15)	0.211(13)	0.106(39)
Squalane	MD AA	808.3(1.8)	0.2112(23)	0.192(11)
Squalane	MD UA	843.2(2.7)	0.2268(32)	0.210(16)
PAOs	Experiment	818(37)	0.210(27)	0.064(52)
PAOs	MD AA	805.1(1.8)	0.2097(22)	0.177(10)
PAOs	MD UA	844.6(0.0)	0.2065(10)	0.152(02)

The general trends in the current and literature results are consistent, although the current measurements overestimate the literature correlation and extrapolation at high pressure (≥ 1 GPa). The Tait equation of state fitted to the current results is shown in Fig. 5(a), and the fit parameters are given in Table I. Both A and B are in excellent agreement with the literature values with respective deviations of about +5.5% and -11%. Rather than pinning ρ_0 to the ambient-pressure value, it was treated as a fit parameter and it is only 0.79% too low.

A related property is the isothermal compressibility, β . The current experimental results are compared with the literature correlation and extrapolation in Fig. 5(b). The experimental results were computed by direct numerical differentiation. At low pressure, the current experimental results overestimate the literature expression, mainly because of the small number of points in this region. At high pressure, the current experimental results are in excellent agreement with the literature extrapolation to pressures above 0.2 GPa. The value of β is almost zero at about 10 GPa.

Figure 5 also shows the results from MD simulations. First, the AA simulations give accurate values of the density over the whole pressure range, with there being a small underestimation at high pressure. The UA simulations overestimate the density over the whole pressure range, with the relative deviation decreasing with increasing pressure. Fitting the Tait equation of state to both sets of results gives the parameters reported in Table I. With the AA force field, ρ_0 , A , and B deviate from the literature-correlation parameters by +0.36%, +5.6%, and +61%, respectively; with the UA force field, these deviations are +4.7%, +13%, and +76%, respectively. The isothermal compressibility was calculated directly in an MD simulation at each pressure using the standard fluctuation formula⁵¹

$$\beta = \frac{\langle V^2 \rangle - \langle V \rangle^2}{k_B T \langle V \rangle}. \quad (6)$$

These points are plotted in Fig. 5(b). The AA force field is more accurate than the UA force field, and with both force fields, the decrease in compressibility with increasing pressure is correct. Given that the literature correlation covers such a wide temperature and pressure range, the performance of both force fields is quite good, especially when one considers that they were not designed to cope with such extreme conditions. Deviations in the mass density of a few percent are tolerable for the current purposes.

On the basis of the literature correlation and MD simulations, the compressibility starts to decrease at a pressure $P \simeq B$, the fitted values of which are in the region of 0.1–0.2 GPa. Correspondingly, this is also where density begins to differ significantly from its ambient-pressure value. The current experimental results at low pressure are not very reliable—because of the number of available pressure points—but the behavior at high pressure is consistent with all of the other available data. There is no sharp liquid–solid phase transition apparent from the experimental equation of state, and this is mirrored in the MD simulations.

C. Dynamical properties from MD simulations

Self-diffusion coefficients D were calculated in MD simulations of squalane by computing the average mean squared distance $\langle R^2(t) \rangle$

traveled by each of the atoms as a function of time t . D was then calculated using the Einstein relation,

$$D = \lim_{t \rightarrow \infty} \frac{1}{6} \frac{d\langle R^2 \rangle}{dt}. \quad (7)$$

It is unlikely that the asymptotic, diffusive regime can be reached at the highest pressures and densities. Figure 6(a) shows some examples in the range of 0.1–1 GPa. At the lowest pressure, normal diffusion is achieved within 30 ns. At the highest pressure, the mean-squared displacement looks approximately linear over the course of the simulation, but it is possible that, asymptotically, the slope tends toward zero.

Straight lines were fitted to the data over the ranges $10 \text{ ns} \leq t \leq 30 \text{ ns}$, and the apparent values of D therefore characterize the diffusion over the simulation time scale but maybe not the asymptotic long-time behavior at the highest pressures. The results from MD simulations with both AA and UA force fields are shown in Fig. 6(b) (note the logarithmic scales). The diffusion coefficients are quite insensitive to pressure up to about 0.1 GPa, mirroring the response of the density. The ambient-pressure values of D are $1.7 \times 10^{-11} \text{ m}^2 \text{ s}^{-1}$ (AA) and $1.3 \times 10^{-11} \text{ m}^2 \text{ s}^{-1}$ (UA). These values can be compared with earlier NVT MD simulation results using UA force fields at a similar temperature of $T = 293 \text{ K}$: in Ref. 24, $D = 3.1 \times 10^{-11} \text{ m}^2 \text{ s}^{-1}$ and in Ref. 25, $D = 3.2 \times 10^{-11} \text{ m}^2 \text{ s}^{-1}$ and $3.6 \times 10^{-11} \text{ m}^2 \text{ s}^{-1}$ using two different models. In Ref. 24, it

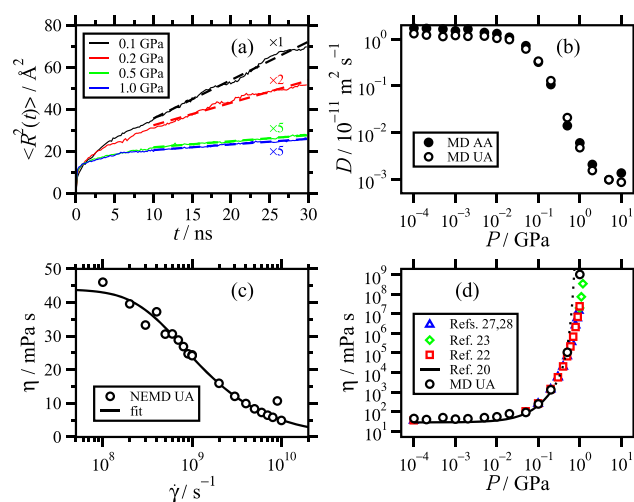


FIG. 6. The dynamical properties of squalane. (a) Mean-squared displacement as a function of time from MD simulations with the AA force field. The dashed lines show the linear fits to Eq. (7), from which the self-diffusion coefficients were obtained. The data at 0.2 GPa, 0.5 GPa, and 1.0 GPa are scaled by factors of 2, 5, and 5, respectively, for clarity. (b) Self-diffusion coefficient as a function of pressure from MD simulations using both the AA and UA force fields. (c) Shear viscosity as a function of shear rate $\dot{\gamma}$ at $P = 1.01325$ bar. The points are from NEMD simulations using the UA force field, and the line is a fit to the Eyring equation (3). (d) The shear viscosity as a function of pressure. The blue triangles are simulation data at 293 K from Refs. 27 and 28. The green diamonds are experimental data at 294.65 K from Ref. 23. The red squares are experimental data at 293.15 K from Ref. 22. The black solid line is an experimental correlation at 298.15 K and up to 0.2 GPa from Refs. 20, and the black dotted line is an extrapolation to higher pressures. The black circles are from the current NEMD simulations using the UA force field.

was noted that *NVT* simulations at the experimental mass density had large, negative pressures, and that “pressure corrections could roughly halve” the values, which would bring them into line with the values obtained here. Experimentally, pulsed field gradient nuclear magnetic resonance (NMR) measurements give $D = 2.7 \times 10^{-11} \text{ m}^2 \text{ s}^{-1}$.²⁴ Here, the dependence on pressure is the primary focus. Figure 6(b) shows that D decreases by about three orders of magnitude over the pressure range 0.01–10 GPa. By about 0.2 GPa, D has already decreased by an order of magnitude from the ambient-pressure value. At the highest pressures, the mobility of the atoms is extremely low and as noted above, the values of D are only indicative of the local motions over a few tens of nanoseconds. Nonetheless, the general trend in D is consistent with the solidification signaled by the equations of state presented in Sec. III A. The overall agreement between the AA and UA simulation results is good. Experimental measurements of the diffusion coefficient would be difficult at high pressures.

The shear viscosity was measured in NEMD simulations using the UA force field. Figure 6(c) shows an example of the shear-rate dependent viscosity at a pressure of 1.013 25 bar. The high- $\dot{\gamma}$ results lie on a smooth curve because the values of P_{xy} and the signal-to-noise ratio are large. The extrapolation to the low- $\dot{\gamma}$ Newtonian regime is not perfect, but even in this case, the error in $\eta(0)$ is likely to be less than $\sim 0.01 \text{ mPa s}$. Figure 6(d) shows η as a function of pressure. Extrapolating the results to ambient pressure P_0 with an exponential function gives $\eta_0 = 43.4 \text{ mPa s}$, which is higher than the experimental value of 27.8 mPa s .²⁰ Also shown in Fig. 6(d) are experimental results at 293.15 K and 294.65 K,^{22,23} simulation results at 293 K,^{27,28} and an experimental correlation/extrapolation.²⁰ The response of the viscosity to pressure can be characterized by two coefficients defined by

$$\alpha_0 = \left. \frac{d \ln \eta}{dP} \right|_{P_0}, \quad (8)$$

$$\alpha^* = \left[\int_{P_0}^{\infty} \frac{\eta_0}{\eta} dP \right]^{-1}, \quad (9)$$

where α_0 reflects the exponential increase in viscosity at low pressure. Simulation results are compared with experimental data at the same or nearby temperatures in Table II. The UA force field overestimates the viscosity as compared to experiments, which is also consistent with the density being higher and the diffusion coefficients being lower than those with the AA force field. Nonetheless, the

values of α_0 and α^* are in reasonable agreement with published values from experiments^{20,22} and simulations^{27,28} with a different UA force field.^{24,25}

D. Structural properties from HPXRD and MD simulations

The next task is to find a molecular-scale explanation for the changes in the equation of state and dynamical properties observed at high pressure. To start, Fig. 7(a) shows HPXRD profiles of squalane at ambient pressure ($\sim 0.0001 \text{ GPa}$) and at 5 GPa. The results are presented as a function of the d spacing. The essential points are that (i) there are no Bragg peaks and (ii) the main peak shifts from around 4.8 \AA at low pressure to about 4.2 \AA at high pressure. A reduction in d spacing is, of course, expected on compression.

To gain insights into the experimental results, the radial distribution functions (RDFs) were computed in MD simulations, using both the AA and UA force fields. Because the x-ray scattering cross section for C is much greater than for H, Fig. 8(a) shows the carbon-carbon RDFs (including bonded pairs) calculated with the UA force field. In all cases, $g(r)$ tends to 1 at large r , showing that there is no long-range order. The changes in the RDF with increasing pressure are subtle. The intermediate-range correlations at 3–5 \AA show some blurring with increasing pressure.

To investigate the short-range and intermediate-range order, the static structure factor was computed from the RDF using the equation

$$S(q) = 1 + 4\pi n \int_0^\infty r^2 \left(\frac{\sin qr}{qr} \right) [g(r) - 1] dr, \quad (10)$$

where $q = 2\pi/d$ is the scattering wave vector and $n = N/V$ is the total concentration of C atoms in the system. The results are shown in Fig. 8(b). There are two dominant peaks, at $q \approx 1\text{--}2 \text{ \AA}^{-1}$ and $q \approx 5\text{--}6 \text{ \AA}^{-1}$, and both shift to higher values of q with increasing pressure, consistent with the compression of the system. Looking at the RDFs in Fig. 8, there is a subtle increase and blurring of the peaks around $r \approx 3.5 \text{ \AA}$. This corresponds to wave vectors $q \approx 2\pi/r = 1.8 \text{ \AA}^{-1}$, meaning the primary peak in $S(q)$.

The peak positions q_{max} are plotted as functions of pressure in Figs. 8(c) and 8(d). These plots show that the peaks shift at pressures above about 0.1 GPa. The differences between the results using AA and UA force fields are small, being 0.2 \AA^{-1} at most, and reflect the relative densities plotted in Fig. 5(a). Given that there is no sharp

TABLE II. Dynamical parameters from experimental and MD simulation results for squalane and PAOs. η_0 is the viscosity at pressure P_0 , and α_0 and α^* are pressure coefficients defined in Eqs. (8) and (9), respectively.

Material	T (K)	Source	η_0 (mPa s)	α_0 (GPa ^{−1})	α^* (GPa ^{−1})
Squalane	293	References 27 and 28	36.5	18.4	18.4
Squalane	293.15	Reference 22	35.9	22.3	19.7
Squalane	298.15	Reference 20	27.8	22.9	19.9
Squalane	298.15	MD UA	43.4	16.7	20.9
PAO trimer	313.15	Reference 21	13.0	20.2	15.0
PAOs	298.15	MD UA	27.3	10.0	10.0

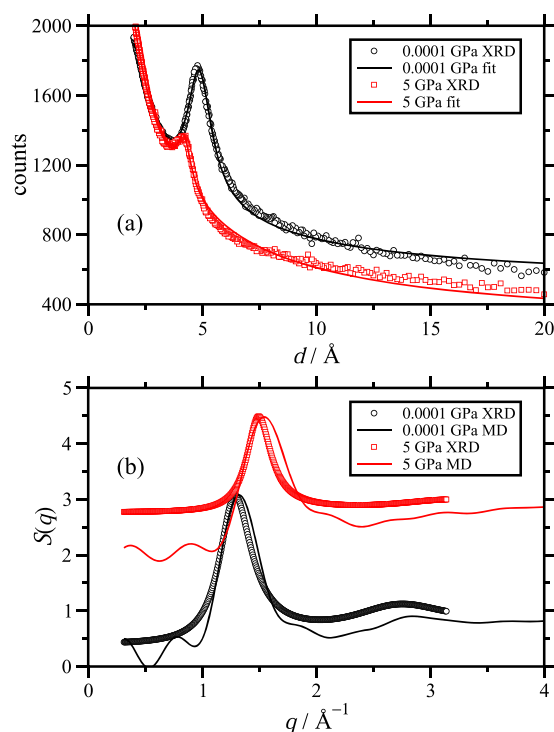


FIG. 7. XRD results from experiment and MD simulation at 0.0001 GPa and 5 GPa. (a) Raw XRD data from experiments, plotted as counts vs d spacing, and fits to Eq. (12). (b) Structure factor from experiments (points) and MD simulations with the UA force field (lines). The results at 0.0001 GPa are shown as black circles and black lines and at 5 GPa as red squares and red lines. The results at 5 GPa are shifted up by one unit for clarity.

liquid–solid transition with increasing pressure, one might expect that the shifts in q_{\max} come about primarily from an isotropic scaling of the system. If this were the case, then distances would be scaled from reference values r_0 and V_0 like $r/V_0^{1/3} = r_0/V_0^{1/3}$ and wave vectors would be scaled like $qV_0^{1/3} = q_0V_0^{1/3}$. The scaling is known from the fitted equation of state. Figures 8(c) and 8(d) show plots of the function

$$\frac{q}{q_0} = \left(\frac{\rho}{\rho_0} \right)^{1/3}, \quad (11)$$

where the density is taken from Eq. (5), and q_0 and ρ_0 are the wave vector and density at pressure P_0 , respectively. These plots show that the changes in $S(q)$ are not simply due to isotropic compression of the system: the density scaling slightly underestimates the shift in the primary peak (representing intermediate-range order) but strongly overestimates the shift in the secondary peak (representing short-range order). Therefore, there must be a structural rearrangement in the system that occurs at high pressure.

Identifying all of the qualitative changes in structure would be difficult, but one obvious candidate could be the conformations of single molecules, as measured by the radius of gyration R_g . A plot

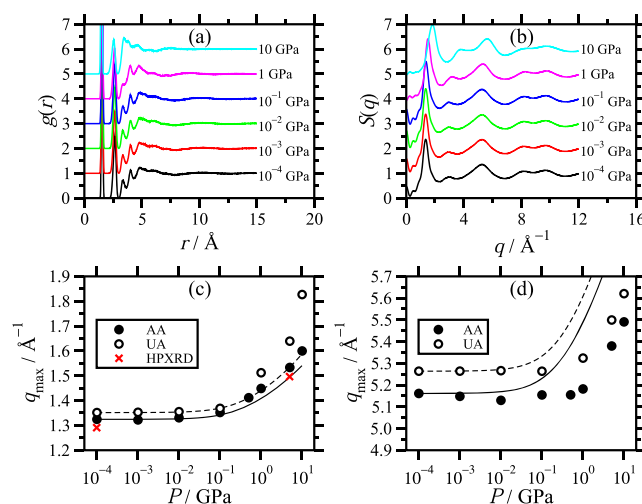


FIG. 8. Structural properties of squalane at $T = 298.15$ K and $P = 10^{-4}$ –10 GPa. (a) Carbon–carbon radial distribution functions $[g(r)]$ from MD simulations with the UA force field. (b) Carbon–carbon static structure factor $[S(q)]$ from MD simulations with the UA force field. (c) Primary peak position and (d) secondary peak position in $S(q)$ from simulations with the AA force field (filled symbols) and the UA force field (unfilled symbols). The solid and dashed lines are the predictions of Eq. (11) for the AA and UA results, respectively. In (a) and (b), the results at each pressure are shifted up by one unit for clarity.

of R_g as a function of pressure from simulations with the UA force field is shown in Fig. 9. At low pressure, R_g increases with increasing pressure (and density) due to the better packing of the molecules in parallel conformations. The ambient-pressure value of $R_g = 6.9$ Å at 298.15 K is consistent with the simulated values of 7.0 Å and 6.5 Å at 293 K reported in Ref. 24. Remarkably, at around 0.1 GPa, R_g decreases sharply, which coincides with the increases in the peak positions in $S(q)$. This “molecular crumpling” effect would lead to more intramolecular contacts between atoms, and this could be connected with the shift in the secondary peak, which corresponds to real-space distances $r \simeq 2\pi/q = 1.1$ –1.2 Å. One can also calculate an effective hydrodynamic radius using the Stokes–Einstein law, $R_h = k_B T / 6\pi\eta D$, and this is shown in Fig. 9. R_h decreases sharply above 0.1 GPa, reflecting the fact that the viscosity increases faster than the diffusion coefficient decreases, as is evident by comparing Figs. 6(b) and 6(d).

Finally, the simulated $S(q)$ is compared with the HPXRD scattering profiles. The following procedure was used to extract the single peak in the experimental results. The measured counts were fitted using a function

$$\text{counts} = a + bq + cf(q), \quad (12)$$

where $q = 2\pi/d$, and a , b , and c are fitting parameters. This was meant to reflect a linear background (when counts are plotted against q), plus a modulating function that resembles the structure factor $S(q)$. The function

$$f(q) = \frac{1}{1 + ru(q)}, \quad (13)$$

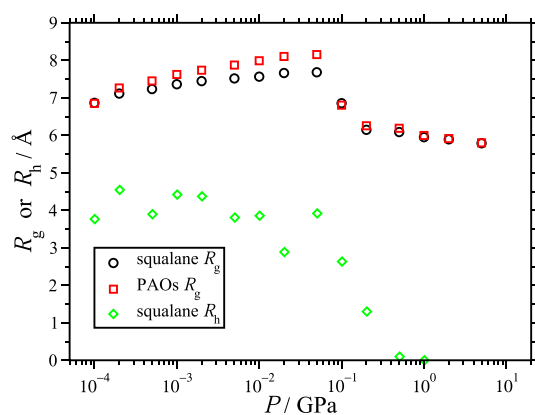


FIG. 9. Radii of gyration of squalane and PAO molecules as functions of pressure at $T = 298.15$ K. Also shown is the effective hydrodynamic radius R_h for squalane, obtained from the Stokes–Einstein relation. The results are from MD simulations with the UA force field.

$$u(q) = \frac{\sin(ql) - (ql)\cos(ql)}{(ql)^3} \quad (14)$$

was chosen heuristically to give a good fit to the peak, where r and l are further fitting parameters. The fits are shown in Fig. 7(a) and, apart from at large d (small q), they are quite good. Figure 7(b) shows $S(q)$ from MD simulations with the AA force field at 0.0001 GPa and 5 GPa, compared to the functions $f(q)$ suitably shifted and scaled along the ordinate only. The low- q oscillations in $S(q)$ are just Fourier-transform truncation errors, and no attempt was made to control those in case the peak position and width were affected. The aim here is simply to show that the peak position and its dependence on pressure can be obtained consistently from HPXRD and MD simulations. The widths of the peaks are also comparable. The interesting HPXRD fit parameters are the lengths $l = 4.47$ Å at 0.0001 GPa and $l = 3.85$ Å at 5 GPa; these dictate the primary peak positions in $f(q)$ at $q = 1.29$ Å⁻¹ and 1.49 Å⁻¹, respectively. These values are indicated in Fig. 8(c), and they follow the same trends seen in simulations.

In summary, a combined experimental and simulation study of the equation of state, dynamics, and structure of squalane at high pressure shows that it undergoes a crossover to a solid-like state, but without crystallization. Of course, a crystalline phase must be the thermodynamically stable state at very high pressures, but the essential point is that crystallization is not observed even on the experimental time scale. Moreover, at very high pressures, the system undergoes structural arrest, meaning that the amorphous solid becomes a metastable state.

IV. RESULTS: POLY- α -OLEFINS

The aim of this section is to summarize high-pressure results for a mixture of PAOs, showing that the crossover to a high-pressure amorphous solid may be a more general phenomenon in complex hydrocarbons. Figure 10 shows the standard deviation of the pressure, as measured in DAC experiments. Fitting Eq. (4) to the data gives $P^* = 1.34(37)$ GPa, $f_0 = 0.0132(28)$ GPa, $f_1 = 0.085(12)$, and

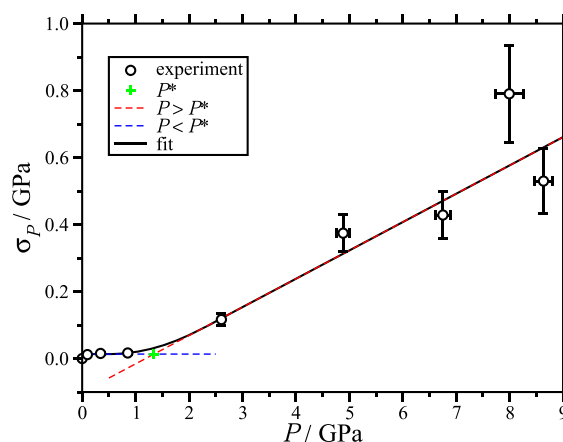


FIG. 10. Pressure dependence of the standard deviation, σ_P , for PAOs at $T \approx 298$ K. The points are from the experiment, and the black solid line is the fit from Eq. (4). The blue and red dashed lines show the limiting behavior at low pressure and high pressure, respectively, and the two intersect at $P^* \approx 1.3$ GPa, shown by a green cross.

$\Delta P = 0.86(53)$ GPa. The number of points does not permit a more precise determination of the fit parameters, but it is estimated that the boundary between the hydrostatic and non-hydrostatic regimes is around 1.3 GPa and that the liquid begins to solidify at a pressure $P^* - \Delta P \approx 0.5$ GPa.

The equation of state is shown in Fig. 11(a), along with results from MD simulations with both AA and UA force fields. As in the experiments with squalane, the mass of the sample is not known precisely. In the absence of literature data on the mass density of this mixture, the experimental data have been scaled to match the mass density from MD simulations under ambient conditions. This is adequate for detecting any rapid changes in density. The results are similar to those for squalane, in that the density begins to increase at about 0.1 GPa and that the UA force field gives a higher density than the AA force field. All of the results were fitted with the Tait equation of state, and the fit parameters are given in Table I. The parameter A is consistent across the experiments and both sets of simulations. The parameter B is consistent between both sets of simulations, while the experimental value is considerably lower due to the lack of measurements at low pressure, and the corresponding overestimation of the initial increase in ρ .

The isothermal compressibility is shown in Fig. 11(b). There is excellent agreement between simulations with the UA and AA force fields above 0.1 GPa, while the UA force field gives a lower compressibility at lower pressures. The experimental results are consistent with the simulations at high pressure.

Figures 11(c) and 11(d) show the self-diffusion coefficient and shear viscosity from MD simulations. D decreases by several orders of magnitude over the pressure range considered. The agreement between the results using AA and UA force fields is good. The shear viscosity from NEMD simulations with the UA force field is plotted as a function of pressure; the fit parameters are given in Table II. Also shown are experimental data for the pure trimer of dec-1-ene at 313.15 K,²¹ which are the closest available in the literature. The simulation and experimental results are qualitatively

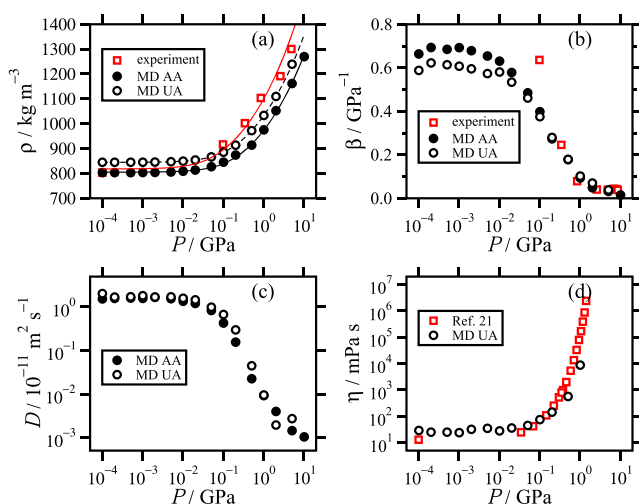


FIG. 11. The equation of state and dynamical properties of PAOs. (a) The mass density as a function of pressure. The lines are fits using the Tait equation of state [Eq. (5)]. (b) The isothermal compressibility as a function of pressure. In (a) and (b), the red squares are from the DAC experiments. (c) Self-diffusion coefficient as a function of pressure from MD simulations. (d) The shear viscosity as a function of pressure. The red squares are experimental data for the pure decene trimer at $T = 313.15$ K from Ref. 21. In (a)–(d), the filled and unfilled black circles are from NEMD simulations using the AA and UA force fields, respectively.

similar, although the fitted values of η_0 , α_0 , and α^* from simulations are poor, as calculations were not carried out over the full pressure range. The radius of gyration, plotted in Fig. 9, shows that the changes in density, compressibility, diffusion coefficient, and viscosity above 0.1 GPa are accompanied by the molecular conformations becoming more compact.

The outcome from this part of the work is that the thermodynamic, dynamic, and structural phenomena associated with the solidification of squalane and PAOs at high pressure are very similar. To some extent, this is unsurprising, because all of the molecules are branched and of a similar molecular weight and chemical composition. Nonetheless, this may mean that these phenomena are common to a very broad range of components found in lubricant oils and, therefore, that the crossover to a non-hydrostatic medium is something that occurs in all such systems.

V. CONCLUSIONS

In this work, high-pressure experiments and MD simulations have been used to explore the equation of state, dynamical properties, and molecular-scale ordering in some hydrocarbons that are good models for lubricant base oils. All results are for room temperature, to facilitate the comparison between high-pressure experiments and simulations. As a general rule, above about 0.1 GPa, the density, isothermal compressibility, self-diffusion coefficient, and viscosity deviate significantly from their ambient-pressure values. In the case of squalane, it is possible that this occurs as the system crosses the glass-transition line in the phase diagram. At the highest pressures, above 1 GPa, the system is essentially solid: it is clearly a non-hydrostatic medium, and in the MD simulations, diffusion has ceased and the viscosity is extremely high. Crucially,

XRD experiments show that there are no Bragg peaks at high pressure, indicating that the oils remain amorphous. The computed structural properties indicate a change in the local ordering of atoms above 0.1 GPa and an associated collapse of the molecular conformation. Moreover, the computed scattering intensity is in excellent agreement with XRD results at low and high pressures. This shows that, even on the experimental time scale, the system does not crystallize at high pressure and, given that diffusion has basically ceased, the resulting amorphous solid is a metastable state.

The solidification of a lubricant base oil is important in terms of its load-bearing ability in an asperity contact, although the effects of confinement could be just as important as the load itself.⁵² However, what is clear is that, under the conditions typically found in certain parts of engines, the basic physical properties of the base oil are very different from those under ambient conditions. Although this study was carried out at room temperature, as opposed to typical engine temperatures, it has produced some insight into what happens to such liquids at extreme pressure.

ACKNOWLEDGMENTS

The authors would like to acknowledge the funding and technical support from BP through the BP International Centre for Advanced Materials (BP-ICAM), which made this research possible. The project received support from BP International Ltd. and EPSRC through an NPIF studentship to I.J.P. (Project Reference Nos. 2112591 and EP/R512242/1) and the Prosperity Partnership *Preventing Surface Degradation in Demanding Environments* (Project Reference No. EP/R00496X/1). The computational work was supported by access to the BP Center for High-Performance Computing, Houston, Texas.

REFERENCES

- 1 R. A. Mufti and M. Priest, "Effect of engine operating conditions and lubricant rheology on the distribution of losses in an internal combustion engine," *J. Tribol.* **131**, 041101 (2009).
- 2 K. Holmberg, P. Andersson, N.-O. Nylund, K. Mäkelä, and A. Erdemir, "Global energy consumption due to friction in trucks and buses," *Tribol. Int.* **78**, 94–114 (2014).
- 3 R. S. Dwyer-Joyce, T. Reddyhoff, and J. Zhu, "Ultrasonic measurement for film thickness and solid contact in elastohydrodynamic lubrication," *J. Tribol.* **133**, 031501 (2011).
- 4 P. Carden, C. Pisani, J. Andersson, I. Field, E. Lainé, J. Bansal, and M. Devine, "The effect of low viscosity oil on the wear, friction and fuel consumption of a heavy duty truck engine," *SAE Int. J. Fuels Lubr.* **6**, 311–319 (2013).
- 5 V. Macián, B. Tormos, S. Ruíz, and L. Ramírez, "Potential of low viscosity oils to reduce CO₂ emissions and fuel consumption of urban buses fleets," *Transp. Res. D* **39**, 76–88 (2015).
- 6 V. Macián, B. Tormos, S. Ruíz, G. Miró, and T. Pérez, "Evaluation of low viscosity engine wear effects and oil performance in heavy duty engines fleet test," in *SAE 2014 International Powertrain, Fuels and Lubricants Meeting* (SAE International, 2014), Technical Paper 2014-01-2797.
- 7 D. A. Kofke and P. G. Bolhuis, "Freezing of polydisperse hard spheres," *Phys. Rev. E* **59**, 618–622 (1999).
- 8 Y. Su, G. Liu, B. Xie, D. Fu, and D. Wang, "Crystallization features of normal alkanes in confined geometry," *Acc. Chem. Res.* **47**, 192–201 (2014).
- 9 J. Klein and E. Kumacheva, "Confinement-induced phase transitions in simple liquids," *Science* **269**, 816–819 (1995).

- ¹⁰H. Gao and M. Müser, "Why liquids can appear to solidify during squeeze-out—Even when they don't," *J. Colloid Interface Sci.* **562**, 273–278 (2020).
- ¹¹B. O. Jacobson and P. Vinet, "A model for the influence of pressure on the bulk modulus and the influence of temperature on the solidification pressure for liquid lubricants," *J. Tribol.* **109**, 709–714 (1987).
- ¹²M. S. Torikachvili, S. K. Kim, E. Colombier, S. L. Bud'ko, and P. C. Canfield, "Solidification and loss of hydrostaticity in liquid media used for pressure measurements," *Rev. Sci. Instrum.* **86**, 123904 (2015).
- ¹³API Engine Oil Licensing and Certification System, American Petroleum Institute API1509, 18th ed, June 2019, available at: <https://www.api.org/products-and-services/engine-oil/documents/api-1509-documents>; accessed 30 October 2019.
- ¹⁴M. Tsujimoto, "A highly unsaturated hydrocarbon in shark liver oil," *J. Ind. Eng. Chem.* **8**, 889–896 (1916).
- ¹⁵S. K. Kim and F. Karadeniz, "Biological importance and applications of squalene and squalane," *Adv. Food Nutr. Res.* **65**, 223–233 (2012).
- ¹⁶R. Rissmann, M. H. M. Oudshoorn, E. Kocks, W. E. Hennink, M. Ponc, and J. A. Bouwstra, "Lanolin-derived lipid mixtures mimic closely the lipid composition and organization of vernix caseosa lipids," *Biochim. Biophys. Acta Biomembr.* **1778**, 2350–2360 (2008).
- ¹⁷J. Rumble, *CRC Handbook of Chemistry and Physics*, 100th ed. (CRC Press; Taylor & Francis Group, Boca Raton, FL, 2019).
- ¹⁸A. Porras-Vazquez, L. Martinie, P. Vergne, and N. Fillot, "Independence between friction and velocity distribution in fluids subjected to severe shearing and confinement," *Phys. Chem. Chem. Phys.* **20**, 27280–27293 (2018).
- ¹⁹M. J. P. Comuñas, X. Paredes, F. M. Gaciño, J. Fernández, J.-P. Bazile, C. Boned, J.-L. Daridon, G. Galliero, J. Pauly, and K. R. Harris, "Viscosity measurements for squalane at high pressures to 350 MPa from $t = (293.15 \text{ to } 363.15) \text{ K}$," *J. Chem. Thermodyn.* **69**, 201–208 (2014).
- ²⁰S. K. Mylona, M. J. Assael, M. J. P. Comuñas, X. Paredes, F. M. Gaciño, J. Fernández, J. P. Bazile, C. Boned, J. L. Daridon, G. Galliero, J. Pauly, and K. R. Harris, "Reference correlations for the density and viscosity of squalane from 273 to 473 K at pressures to 200 MPa," *J. Phys. Chem. Ref. Data* **43**, 013104 (2014).
- ²¹S. Bair, "The high pressure rheology of some simple model hydrocarbons," *Proc. Inst. Mech. Eng., Part J* **216**, 139–149 (2002).
- ²²S. Bair, "Reference liquids for quantitative elastohydrodynamics: Selection and rheological characterization," *Tribol. Lett.* **22**, 197–206 (2006).
- ²³S. S. Bair, I. Andersson, F. S. Qureshi, and M. M. Schirru, "New EHL modeling data for the reference liquids squalane and squalane plus polyisoprene," *Tribol. Trans.* **61**, 247–255 (2018).
- ²⁴M. Mondello and G. S. Grest, "Molecular dynamics of linear and branched alkanes," *J. Chem. Phys.* **103**, 7156–7165 (1995).
- ²⁵M. Mondello, G. S. Grest, A. R. Garcia, and B. G. Silbernagel, "Molecular dynamics of linear and branched alkanes: Simulations and nuclear magnetic resonance results," *J. Chem. Phys.* **105**, 5208–5215 (1996).
- ²⁶S. Bair, C. McCabe, and P. T. Cummings, "Comparison of nonequilibrium molecular dynamics with experimental measurements in the nonlinear shear-thinning regime," *Phys. Rev. Lett.* **88**, 058302 (2002).
- ²⁷V. Jadhao and M. O. Robbins, "Probing large viscosities in glass-formers with nonequilibrium simulations," *Proc. Natl. Acad. Sci. U. S. A.* **114**, 7952–7957 (2017).
- ²⁸V. Jadhao and M. O. Robbins, "Rheological properties of liquids under conditions of elastohydrodynamic lubrication," *Tribol. Lett.* **67**, 66 (2019).
- ²⁹S. A. Gupta, H. D. Cochran, and P. T. Cummings, "Shear behavior of squalane and tetracosane under extreme confinement. I. Model, simulation method, and interfacial slip," *J. Chem. Phys.* **107**, 10316–10326 (1997).
- ³⁰S. A. Gupta, H. D. Cochran, and P. T. Cummings, "Shear behavior of squalane and tetracosane under extreme confinement. II. Confined film structure," *J. Chem. Phys.* **107**, 10327–10334 (1997).
- ³¹S. A. Gupta, H. D. Cochran, and P. T. Cummings, "Shear behavior of squalane and tetracosane under extreme confinement. III. Effect of confinement on viscosity," *J. Chem. Phys.* **107**, 10335–10343 (1997).
- ³²M. Doig, C. P. Warrens, and P. J. Camp, "Structure and friction of stearic acid and oleic acid films adsorbed on iron-oxide surfaces in squalane," *Langmuir* **30**, 186–195 (2014).
- ³³G. Tsagaropoulou, C. P. Warrens, and P. J. Camp, "Interactions between friction modifiers and dispersants in lubricants: The case of glycerol monooleate and polyisobutylsuccinimide-polyamine," *ACS Appl. Mater. Interfaces* **11**, 28359–28369 (2019).
- ³⁴G. J. Piermarini, S. Block, J. D. Barnett, and R. A. Forman, "Calibration of the pressure dependence of the R_1 ruby fluorescence line to 195 kbar," *J. Appl. Phys.* **46**, 2774–2780 (1975).
- ³⁵K. Syassen, "Ruby under pressure," *High Pressure Res.* **28**, 75–126 (2008).
- ³⁶S. Klotz, J.-C. Chervin, P. Munsch, and G. Le Marchand, "Hydrostatic limits of 11 pressure transmitting media," *J. Phys. D: Appl. Phys.* **42**, 075413 (2009).
- ³⁷S. K. Gupta, "Peak decomposition using Pearson type VII function," *J. Appl. Cryst.* **31**, 474–476 (1998).
- ³⁸S. Nadarajah and S. Kotz, "A product Pearson-type VII density distribution," *J. Comput. Appl. Math.* **211**, 103–113 (2008).
- ³⁹H. K. Mao, J. Xu, and P. M. Bell, "Calibration of the ruby pressure gauge to 800 kbar under quasi-hydrostatic conditions," *J. Geophys. Res.* **91**, 4673–4676, <https://doi.org/10.1029/jb091ib05p04673> (1986).
- ⁴⁰O. A. Nerushev, G. Dowd, and C. R. Pulham, "Determination of the freezing pressures and compressibilities of selected lubricants using multi-ruby fluorescence and optical techniques" (unpublished) (2020).
- ⁴¹M. Basham, J. Filik, M. T. Wharmby, P. C. Y. Chang, B. El Kassaby, M. Gerring, J. Aishima, K. Levik, B. C. A. Pulford, I. Sikharulidze, D. Sneddon, M. Webber, S. S. Dhesi, F. Maccherozzi, O. Svensson, S. Brockhauser, G. Náray, and A. W. Ashton, "Data analysis workbench (DAWN)," *J. Synchrotron Radiat.* **22**, 853–858 (2015).
- ⁴²See <http://lammps.sandia.gov> for LAMMPS Molecular Dynamics Simulator, 1995.
- ⁴³S. Plimpton, "Fast parallel algorithms for short-range molecular dynamics," *J. Comput. Phys.* **117**, 1–19 (1995).
- ⁴⁴L. Martinez, R. Andrade, E. G. Birgin, and J. M. Martinez, "PACKMOL: A package for building initial configurations for molecular dynamics simulations," *J. Comput. Chem.* **30**, 2157–2164 (2009).
- ⁴⁵W. L. Jorgensen, J. D. Madura, and C. J. Swenson, "Optimized intermolecular potential functions for liquid hydrocarbons," *J. Am. Chem. Soc.* **106**, 6638–6646 (1984).
- ⁴⁶W. L. Jorgensen and J. Tirado-Rives, "The OPLS potential functions for proteins. energy minimizations for crystals of cyclic peptides and crambin," *J. Am. Chem. Soc.* **110**, 1657–1666 (1988).
- ⁴⁷W. L. Jorgensen, D. S. Maxwell, and J. Tirado-Rives, "Development and testing of the OPLS all-atom force field on conformational energetics and properties of organic liquids," *J. Am. Chem. Soc.* **118**, 11225–11236 (1996).
- ⁴⁸D. J. Evans and G. P. Morriss, "Nonlinear-response theory for steady planar Couette flow," *Phys. Rev. A* **30**, 1528–1530 (1984).
- ⁴⁹P. J. Davis and B. D. Todd, "A simple, direct derivation and proof of the validity of the SLLOD equations of motion for generalized homogeneous flows," *J. Chem. Phys.* **124**, 194103 (2006).
- ⁵⁰D. M. Heyes, D. Dini, and E. R. Smith, "Incremental viscosity by non-equilibrium molecular dynamics and the Eyring model," *J. Chem. Phys.* **148**, 194506 (2018).
- ⁵¹M. P. Allen and D. J. Tildesley, *Computer Simulation of Liquids*, 2nd ed. (Oxford University Press, Oxford, 2016).
- ⁵²S. Bair, "The viscosity at the glass transition of a liquid lubricant," *Friction* **7**, 86–91 (2019).